



Progressive fracture processes around tunnel triggered by blast disturbances under biaxial compression with different lateral pressure coefficients

Yi LONG, Jian-po LIU, Gang LEI, Ying-tao SI, Chang-yin ZHANG, Deng-cheng WEI, Hong-xu SHI

Key Laboratory of Ministry of Education on Safe Mining of Deep Metal Mines,
Northeastern University, Shenyang 110819, China

Received 11 January 2020; accepted 22 June 2020

Abstract: To investigate the progressive fracture processes around a tunnel triggered by static stress and dynamic disturbance, experiments and numerical simulations were performed. The results show that the spatial distributions of acoustic emission (AE) events become very different as lateral pressure coefficients change. The combined effect of static stress and dynamic disturbance causes the damage around the tunnel, and initial stress conditions control the damage morphology. The blast disturbance cannot fundamentally change the damaged area but will deepen the extent of damage and accelerate the failure speed. The more significant the difference between the vertical and horizontal stresses is, the higher the impact on the tunnel by the dynamic disturbance is. The AE activity recovers to a relatively stable state within a short time after the blast and conforms to power-law characteristics.

Key words: tunnel damage; blast disturbance; lateral pressure coefficient; acoustic emission; power-law fitting

1 Introduction

Under high in-situ stress conditions, in the mining process, rock masses are inevitably subjected to frequent disturbances that can be classified into unloading effects, i.e., the stress change in the surrounding rock mass after the ore is mined, and dynamic disturbances, such as blast. Therefore, the rock mass is subjected to high stress and dynamic disturbance [1]. For high-production mines, especially those that use medium-length hole blast or long-hole blast, one uses more than hundreds of kilograms or even several tons of explosives. Strong blast disturbances can easily lead to spalling and collapse of the surrounding rock of tunnels, even generating dynamic hazards, such as

rockbursts [2–5]. Statistical data show that two-thirds of mine rockbursts occur after blasts. For example, blast vibrations damaged more than 20 m of the roadway in the Hongtoushan copper mine, one of the deepest nonferrous metal mines in China, at a mining depth of 1000 m [6]. In the Gujiatai iron mine, a blast disturbance caused the collapse of a large rock mass in a stope, and the production was subsequently suspended for several years, resulting in severe economic losses. During the deep tunnel excavation of the Jinping II hydropower station, a blast disturbance caused a time-delayed rockburst, for which the height, length, and maximum depth of the damage were 4, 30, and 0.9 m, respectively [7].

In deep rock masses, stresses quite possibly concentrate around the tunnel. As a result, the triggering effect of dynamic disturbance for rock

Foundation item: Project (2017YFC0602904) supported by the National Key Research and Development Program of China; Project (51974059) supported by the National Natural Science Foundation of China; Project (N180115010) supported by the Fundamental Research Funds for the Central Universities, China

Corresponding author: Jian-po LIU; Tel: +86-13514265478; E-mail: liujianpo@mail.neu.edu.cn
DOI: 10.1016/S1003-6326(20)65398-5

damage is more prominent under such conditions. At present, the research on the excavation-damage zone (EDZ) of tunnels is mainly conducted under static loading using rigid or servo-controlled testing machines. However, the damage in rock mass induced by dynamic disturbances cannot be ignored, especially under high in-situ stress conditions [8]. The split Hopkinson pressure bar (SHPB) is a commonly-used device for studying the characteristics of rock dynamics. With the help of the SHPB, many researchers [9–11] have tested the dynamic strength of rocks and subsequently established constitutive relations and proposed many models based on fracture mechanics or damage mechanics. In addition to the SHPB device, several other instruments have been developed to simulate the deformation and failure evolution under dynamic disturbance [12–16]. Numerical simulation was also performed by ZHU et al [8,17] and LI et al [18] to evaluate the dynamic stress concentration around the tunnel, and the areas prone to failure induced by dynamic disturbance were found. However, experimental works on rock damage due to dynamic disturbances are mainly restricted to surface observations, and the evolution characteristics of internal damage still need to be further studied. When a rock is subjected to loading conditions, microcracks gradually generate, propagate and coalesce, accompanied by a release of elastic strain energy, i.e., acoustic emission (AE). The AE technique can continuously monitor the temporal-spatial evolution of microcracks, thereby revealing the deformation and failure process of rock. A series of achievements have been realized, e.g., the AE location algorithms, the temporal-spatial evolution of microcracks in rock bodies, and the changes in many AE parameters [19–32].

In this study, cement mortar was used to create specimens with a prefabricated circular hole in the middle. The biaxial stress is applied with different lateral pressure coefficients that are calculated from the stress condition around a tunnel in the Ashele copper mine, and the blast method is used to generate dynamic disturbances. In this process, the spatial-temporal evolution of the AE activity was analyzed to reveal the damage characteristics under static stress and blast disturbance conditions. Also, numerical simulations were performed to verify the experimental results, to provide a theoretical basis for support optimization for deep tunnels.

2 Experimental

2.1 Specimen preparation and AE monitoring scheme

The specimens used in this work were made of cement mortar of 300 mm × 300 mm ($L \times W$), 250 mm in thickness (Fig. 1). The mass ratio of cement to sand and water was 1:4.1:0.9. A circular hole with a diameter of 57 mm was drilled in the middle of each specimen. Also, specimens with the same mass ratio were used to measure the uniaxial compressive strength (UCS), and the results showed that the UCS of this batch of specimens was approximately 24 MPa.

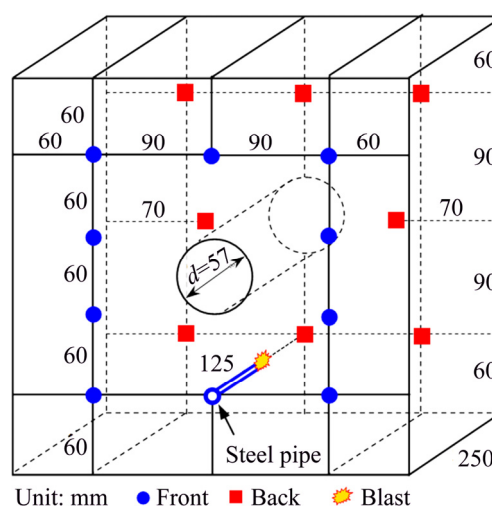


Fig. 1 Specimen structure, AE sensor arrangement, and blast position

Seventeen sensors with a response frequency range of 50–400 kHz were arranged on the front and back faces of the specimens, eight on the front face, and nine on the back face. When the sensors were fixed on the specimen faces, rubber bands and vaseline were used for coupling between sensors and specimen. A sensor highway-II (SH-II, American Physical Acoustics Corp.) system was used for the AE monitoring. The system uses an 18-bit A/D switching technology that allows instant time waveform recording with a maximum upper limit amplitude of ± 10 V. The sampling threshold, sampling frequency, and sampling length were set to be 45 dB, 10 MHz and 5120, respectively.

2.2 Blast disturbance scheme

The blast position was located in the middle of the specimen, 60 mm away from the bottom face

(Fig. 1). When the explosive was detonated, the detonation gas and shock waves could quickly induce ruptures around the blast hole that may propagate and extend to the tunnel, thereby causing failure around the tunnel. The explosive was placed in a steel pipe with a bottom closed-end to avoid the blast breaking the specimen. The diameter, thickness, and length of the steel pipe were 8, 0.1, and 125 mm, respectively. The explosives were prepared by mixing cyclonite with potassium picrate because the cyclonite has high brisance and low sensitivity, while the potassium picrate has opposite characteristics. The optimized mass ratio of the two materials was 1:1 as obtained from a preliminary test. Each blast used 1 g of explosive. After the explosives were placed in the steel pipe, fine sand was used to fill the blast hole, and electric blast was adopted.

2.3 Loading path

The actual stress condition around the tunnel during the mining process determines the lateral pressure coefficients during biaxial compression. The Ashele copper mine is located in the Xinjiang Uygur autonomous region of China. Currently, the development depth and mining depth are 1200 and 900 m, respectively. The tectonic stress is dominant and increases with the mining depth. According to the stress test results, the horizontal stress is 1.4 times the vertical stress when the mining depth exceeds 800 m from the surface. Under high-stress conditions and blast disturbances, ground hazards, such as spalling, collapse, and rockbursts, frequently occur. Figure 2 shows the vertical stress distribution around the tunnel by the unloading effect of No. 4 stope mining at the 0 m level (approximately 900 m in mining depth) in the Ashele copper mine. Because the stope is vertical, the unloading effect on the horizontal stress is small. From Fig. 2(a), the vertical stress increases from the boundary of the No. 4 stope (position P1) to the maximum value (position P5) and then gradually returns to the in-situ stress level (position P13). Figure 2(b) shows the change in the lateral pressure coefficient k , i.e., the ratio of the vertical stress to the horizontal stress, within 60 m from the stope boundary. Because the lateral pressure coefficient of the in-situ stress is 1.4, in this study, four lateral pressure coefficients were investigated, i.e., 0.8, 1.0, 1.2, and 1.4. The horizontal stresses

(σ_2) were designed to be 16 MPa, and the vertical stresses (σ_1) were designed to be 20, 16, 13.3, and 11.4 MPa, as shown in Fig. 3 and Table 1. The experiment is divided into three stages. First, σ_3 and σ_1 were simultaneously loaded at 3 MPa/min until the predetermined values were reached. Second, six blast disturbances were carried out, and each blast process was conducted after the AE signals stopped generating. Eventually, the vertical stress σ_1 or horizontal stress σ_2 was loaded again until the specimen failed.

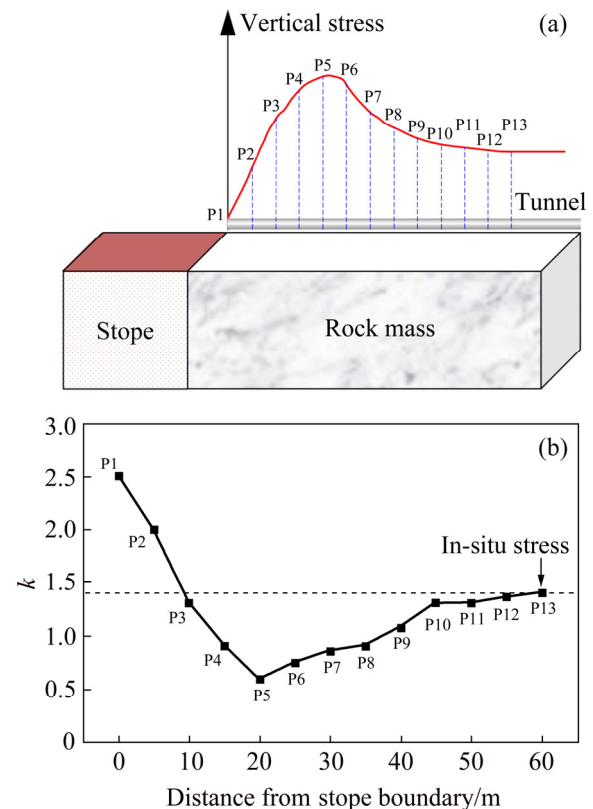


Fig. 2 Schematic diagram of stress distribution around tunnel induced by unloading effect of deep stope mining in Ashele copper mine: (a) Vertical stress distribution; (b) Lateral pressure coefficients, k , in surrounding rock mass of tunnel at different distances from stope

3 AE sequence with loading and blast disturbances

3.1 Filtering of blast signals

At the time of the blast, the stress wave is transmitted to the specimen through the steel pipe and propagates into the specimen. With the high-energy blast trigger stress waves, the waves may continue to propagate in the specimen for some time, and they may be mixed into the signals

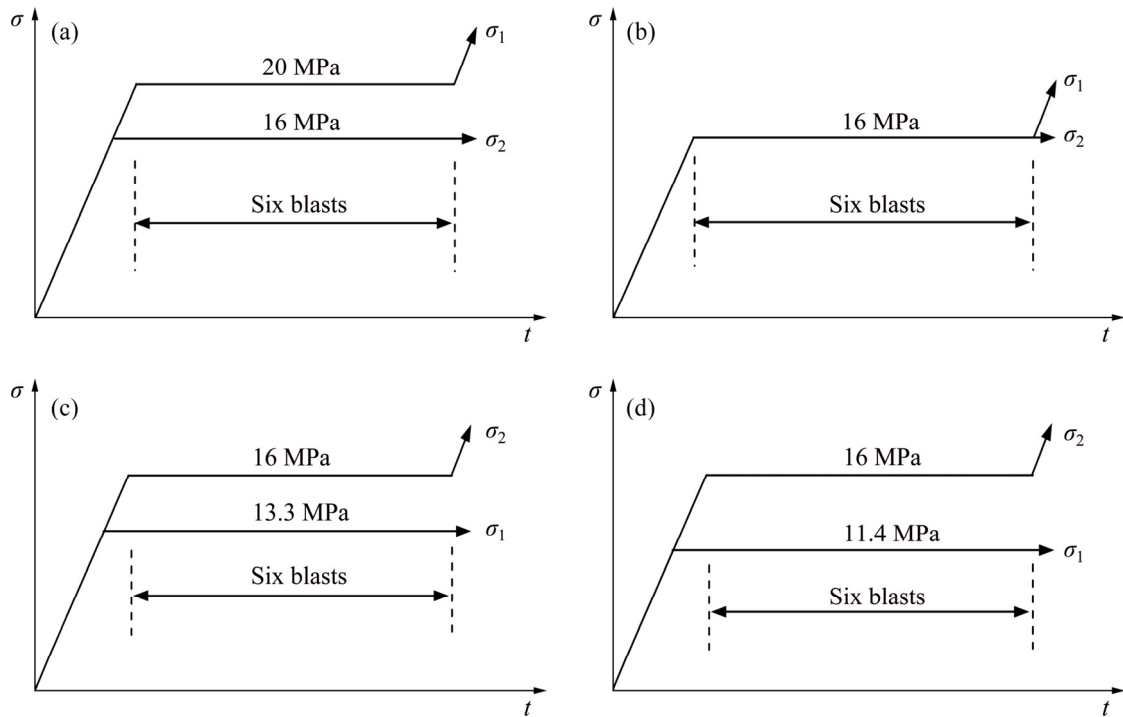


Fig. 3 Schematic diagram of loading path and blast scheme: (a) $k=0.8$; (b) $k=1.0$; (c) $k=1.2$; (d) $k=1.4$

Table 1 Loading plan and blast parameters

Loading plan	Horizontal stress, σ_2 /MPa	Vertical stress, σ_1 /MPa	Blast number	Explosive mass/g	k
1	16	20	6	1	0.8
2	16	16	6	1	1.0
3	16	13.3	6	1	1.2
4	16	11.4	6	1	1.4

generated from microcracks. Therefore, these interference signals should be filtered before analyzing the AE activity. Automatic methods are beneficial to the waveform identification [33–35], especially for large amounts of signal data. However, this study performs manual filtering of blast signals because there are only six blasts for each specimen, and the blast time is known. Also, the process of filtering the interference signals due to blast considers the difference of the parameters between signals induced by blast and microcrack generation and the attenuation law of blast signals.

Due to the considerable amount of explosive energy released during detonation, some parameters of the blast signals such as the rising time, hits, energy, amplitude, and duration time, are very high. Especially, the energy and amplitude of the many blast signals that exceed the acquisition range of the

AE system reach significant values. For example, the amplitude of the typical blast signal shown in Fig. 4(a) is so large that a peak clipping phenomenon appears (the acquisition range of the

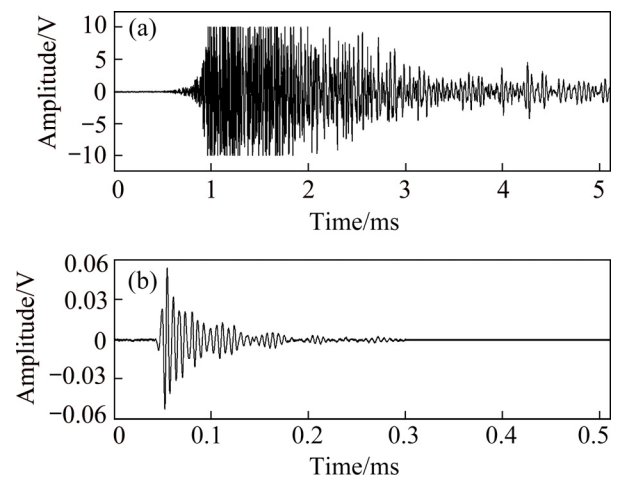


Fig. 4 Waveforms of blast signal (a) and crack signal (b)

amplitude in this AE system is 10 V). Also, the duration time of this blast signal is very long and does not decay to a stable state within the sampling time. On the contrary, the waveform parameters of the signal from the generated microcracks are much lower than those of the blast signal (see Fig. 4(b)). Therefore, the blast signal can be identified and filtered out according to the waveform parameters.

On the other hand, the blast signal gradually weakens during propagation. When its amplitude is smaller than the sampling threshold, the sensors can not detect it. Many factors affect the signal attenuation, including the excitation conditions, wavefront diffusion, absorption attenuation, interfacial reflection, interfacial transmission, and interfacial morphology. Among them, this study focuses on the absorption attenuation and interfacial reflection. The attenuation formula defined by FUTTERMAN [36] is as follows:

$$\alpha = \frac{1}{\Delta x} \ln \frac{A_1}{A_2} \quad (1)$$

where α is the attenuation coefficient, Δx is the propagation distance, A_1 is the amplitude at the source and A_2 is the amplitude after the propagation distance, Δx . For the interfacial reflection factor, the reflection coefficient is related to the wave impedance of the materials on both sides of the interface. The wave impedance at normal incidence can be written as follows:

$$R = \frac{\rho_2 v_2 - \rho_1 v_1}{\rho_2 v_2 + \rho_1 v_1} \quad (2)$$

where R is the reflection coefficient; ρ_1 , v_1 , ρ_2 and v_2 are the densities and the wave propagation velocities of the specimen and the pressure head, respectively; and $\rho_1 v_1$ and $\rho_2 v_2$ are the wave impedances of the two materials ($\text{kg}/(\text{m}^2 \cdot \text{s})$). According to Eqs. (1) and (2), the time that takes for the blast signal amplitude to decay to the sampling threshold is less than 0.5 ms based on the attenuation coefficient and wave impedances of cement mortar and the wave impedances of steel. In summary, one can identify and remove blast signals by considering their parameter characteristics and attenuation law.

3.2 AE sequence characteristics

Figure 5 shows the AE sequence during the specimen fracturing with different lateral pressure

coefficients. The AE activity closely relates to the stress loading and blast disturbance. For the specimen with lateral pressure coefficient $k=0.8$ (Fig. 5(a)), AE signals are continuously generated during the first loading phase, indicating that the internal damage of the specimen gradually increases during this phase. Also, the AE activities show a “strong \rightarrow weak \rightarrow strong” trend. As some tiny air bubbles were probably mixed into the cement mortar during the pouring process, many initial pores would have formed inside the specimens. Therefore, the original pores and damages were closed and had frictional characteristics during the compaction stage, resulting in the higher AE activities. When the specimen entered the elastic deformation stage, the stress exceeded the damage strength of the material in some regions, and some new microcracks formed. However, the AE activity is weaker than that in the compaction stage. As the stress continued to increase, when the specimen reached the later stage of elastic deformation, the microcracks inside the specimen stably extended, and the AE signal reactivated. For the other specimens, all the AE activities weaken in the first loading phase because the three specimens are subjected to smaller external stresses and do not enter the later elastic deformation stage. In the subsequent blast stage, the stress inside the specimens adjusts sharply due to the strong dynamic disturbance, which causes the AE signal to rise sharply. After each blast, the AE activity returns to a relatively stable state very quickly, suggesting that the stress adjustment process caused by blast disturbance is rapid and that the specimens are in a relatively stable state. If a sample reaches the unstable stage after the first loading, the strong blast disturbance can easily result in the whole specimen’s instability failure. During the second loading, the AE activity is higher than that during the first loading, indicating that one cannot ignore the damage caused by the blast disturbance to the specimens. Although the dynamic disturbance does not result in specimen failure, the increased damage inevitably reduces the strength and stability of specimens.

Table 2 lists the number of AE signals during each loading and blast phase and their proportions with respect to the total number of AE signals. For specimens with lateral pressure coefficients of 0.8, 1.0, 1.2, and 1.4, the loading generates 67.41%,

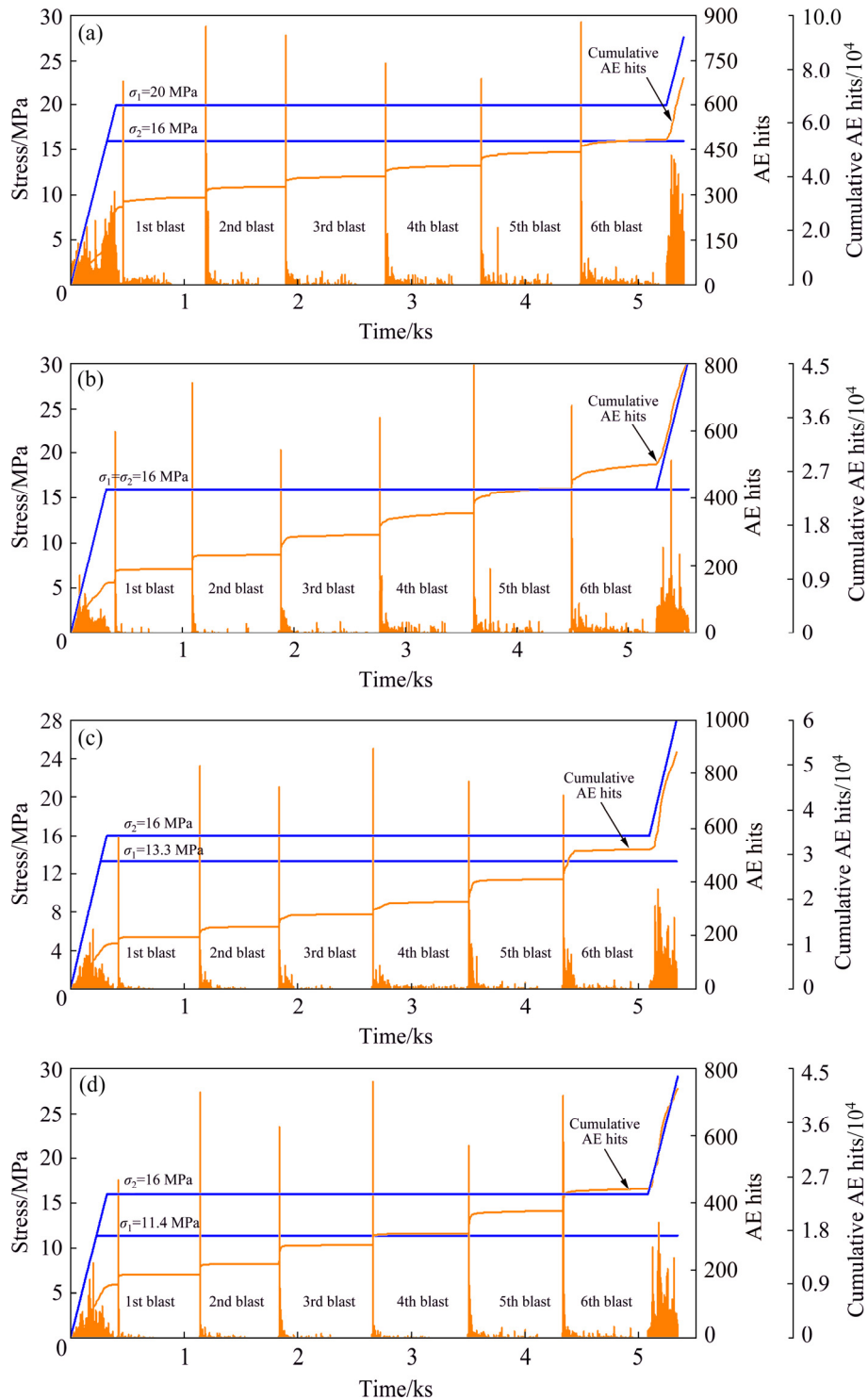


Fig. 5 AE sequence under loading and blast disturbances with different lateral pressure coefficients: (a) $k=0.8$; (b) $k=1.0$; (c) $k=1.2$; (d) $k=1.4$

56.74%, 60.28%, and 61.35% of AE signals, respectively, while the fractions of AE signals related to the blast disturbance are 32.59%, 43.26%, 39.72%, and 38.65%, respectively. These data indicate that the combined effect of static stress and dynamic disturbance causes the damage inside

specimens. It is noted that the number of AE signals generated after each blast gradually increases. According to Table 2, the number of AE signals in the specimen with $k=1.2$ shows a significant growth trend. Because the number of blasts is limited to six, the percentage of damage caused by loading is

Table 2 Numbers of AE signals for each loading and blast phase, and their proportions

<i>k</i>	Phase	Number	Proportion/%	Average proportion/%	Sum	Total proportion/%
0.8	1st load	28973	37.74	–	51748	67.41
	2nd load	22775	29.67			
	1st blast	3355	4.37	5.43	25016	32.59
	2nd blast	4004	5.22			
	3rd blast	3773	4.92			
	4th blast	3936	5.13			
5th blast	4991	6.50				
	6th blast	4957	6.46			
1.0	1st load	8498	18.69	–	25795	56.74
	2nd load	17297	38.05			
	1st blast	2171	4.78	7.21	19665	43.26
	2nd blast	2479	5.45			
	3rd blast	3319	7.30			
	4th blast	3510	7.72			
5th blast	4144	9.12				
	6th blast	4042	8.89			
1.2	1st load	10162	19.22	–	31868	60.28
	2nd load	21706	41.06			
	1st blast	1453	2.75	6.62	21000	39.72
	2nd blast	2190	4.14			
	3rd blast	2759	5.22			
	4th blast	2985	5.65			
5th blast	5008	9.47				
	6th blast	7359	12.49			
1.4	1st load	8814	21.14	–	25575	61.35
	2nd load	16761	40.20			
	1st blast	1704	4.09	6.44	16114	38.65
	2nd blast	1766	4.24			
	3rd blast	3229	7.75			
	4th blast	1928	4.62			
5th blast	3739	8.97				
	6th blast	3748	8.99			

higher than that of blast disturbance. If more blasts are performed, the dynamic disturbance may cause more significant damages, and the specimens may be much more likely to fail during the blast disturbance.

Rock failures and rockbursts during mining excavation can be viewed as a type of earthquake but at a much smaller scale. An earthquake is

large-scale destruction of rock masses in the Earth's crust, and its formation mechanism is similar to the process of microcrack generation and propagation in rock failure processes. Therefore, it might be appropriate to introduce seismology into the study of the rock failure process. After the main earthquake, increased seismic activity (i.e., aftershocks) will be observed, and then the

aftershocks gradually decrease with time and eventually become obscured by the background earthquakes. OMORI [37] discovered scaling in earthquakes in terms of the frequency distribution of aftershocks over one hundred years ago, and subsequently proposed the following formula to represent the decay of aftershock activity with respect to time:

$$N(t)=A(t+c) \tag{3}$$

Equation (3) represents the number of aftershocks $N(t)$, measured at time t after the main earthquake. The terms A and c are constants. This formula and its modified form have been widely used as one of a few established empirical laws in seismology. UTSU [38] modified the Omori’s law by adding the exponent p to describe the power-law decline of aftershocks.

$$N(t)=A(t+c)^{-p} \tag{4}$$

This study regarded the blasts as the main shock and the AE signals within 15 s after blast disturbances as the aftershocks. Since the time from the blast to the generation of microcracks is very short, the parameter c is set to be zero. From Fig. 6 and Table 3, the changes in AE signals after the blasts conform to the power-law characteristics. The p values of 11 blasts are generally greater than 1, indicating that the AE activities recover to a relatively stable state in a short time. The AE activity after blast disturbances can be categorized as the “main shock-after shock” type. SCHOLZ [20] succeeded in reproducing Omori’s power law of the aftershock sequences of AE events in rock specimens. In his experiment, he considered that the fracture of the whole rock specimen corresponds to the main shock and that the AE corresponds to the aftershocks. HIRATA [39] measured a time series of AE in basalt under constant uniaxial

compression, considered some bursts of AE events to be the main shocks, and observed aftershock sequences. The above researches show that AE activity conforms to power-law characteristics regardless of whether static loading or dynamic disturbance is finished; this result can be used to determine the timing of stress adjustment in rock mass quantitatively. For underground tunnel engineering, AE or microseismic (MS) monitoring is proposed to evaluate the rock mass stability for the safety of personnel and equipment.

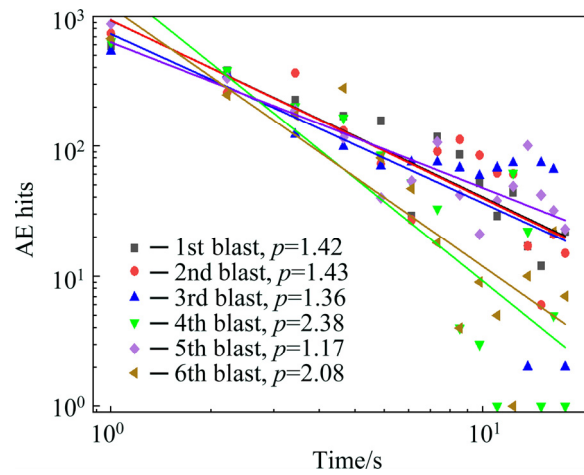


Fig. 6 Power-law decay characteristics of AE activity within 15 s after each blast disturbance ($k=1.0$)

4 Spatial distribution and evolution of AE events, apparent stress, and displacement

4.1 Spatial evolution of AE events

Before the AE source location, the P-wave arrival time was determined. The waveform data can be seen as a time series. The time series of n values is divided into two groups: one of size k values and the other of $n-k$ values. For each value

Table 3 Parameters values of AE activity power-law fitting after each blast disturbance

Blast number	$k=0.8$		$k=1.0$		$k=1.2$		$k=1.4$	
	A	p	A	p	A	p	A	p
1	1318.76	2.08	934.81	1.42	426.36	1.46	1741.99	2.14
2	3512.41	2.58	938.86	1.43	261.39	1.00	677.30	1.67
3	2365.01	2.28	734.70	1.36	507.42	1.11	1067.76	1.22
4	2400.88	2.50	1814.17	2.38	388.53	1.51	1056.77	1.98
5	692.24	1.08	633.81	1.17	482.83	0.75	713.70	0.90
6	2286.80	2.35	1184.68	2.08	340.06	0.59	977.29	1.13

of k , auto-regression (AR) models of the k and $n-k$ data were established, and the Akaike information criterion (AIC, C_{AI}) was adopted to estimate the rationality of the models [40], which is expressed as follows:

$$C_{ap} = C_{AI}^1 + C_{AI}^2 = k \lg e_1^2 + (n-k) \lg e_2^2 + n[\lg(2\pi) + 1] + 2(l_1 + l_2 + 4) \quad (5)$$

where l_1 and e_1 are the degree and variance in the AR model of k values, l_2 and e_2 are the degree and variance in that of $n-k$ data, respectively. The values of C_{ap} for each k are calculated, and the time to the minimum value of C_{ap} can be seen as P-wave arrival time. After that, the simplex method was used to calculate the AE hypocenter position [27,41].

The AE event location analysis attempts to minimize the arrival time difference between the observed and calculated results. With each iterative calculation, the estimated arrival time at the sensor sites is calculated and compared to the observed arrival time, and an estimate of the error is obtained. The absolute deviation method is used to estimate the error as follows:

$$E_r = \left[\frac{1}{N} \sum_{i=1}^N |T_{oi} - T_{ci}| \right] \quad (6)$$

where N is the number of observed arrivals, T_{oi} is the observed arrival time at the i th sensor, and T_{ci} is the estimated arrival time at the i th sensor. Because the wave velocity slows when AE signals pass through the tunnel, the time to reach the sensor is very likely delayed. Thus, the eight earliest arrival times collected by the sensors were used to calculate the AE source location. The result of the pencil-lead break test shows that the location errors of 90% of the events are less than 10 mm, suggesting that the precision of the location can meet the requirements of this study for the temporal-spatial evolution of microcracks.

The distribution and evolution of AE events can directly reflect progressive fracture processes around the tunnel, which have obvious differences among the specimens with different lateral pressure coefficients (Fig. 7). For the specimen with $k=0.8$, many microcracks are generated and concentrated around the tunnel in the first loading phase, and large-scale cracks are mainly distributed on the left and right sides of the circular opening. Then, during the blast phase and the second loading phase, the

AE events continue to concentrate on both sides of the tunnel. Eventually, the AE events show a band-like distribution from the left to the right of the tunnel. For the specimen with $k=1.0$, the stress concentration is evenly distributed around the tunnel because the external horizontal load equals the vertical load. Under this condition, AE events also concentrate around the tunnel during the first loading phase and the blast phase. In the second loading process, a small number of large-scale cracks appear on the left and right sides of the circular opening due to the increase in vertical stress. The spatial distributions of AE events of the two specimens with lateral pressure coefficients k of 1.2 and 1.4 are opposite to that of the specimen with $k=0.8$, for which the AE events are mainly distributed on the upper and lower sides of the circular opening. These results indicate that the lateral pressure coefficients guide the orientation of the initiation and direction of the propagation of microcracks. With the increase in the lateral pressure coefficient, the concentrated area of microcracks gradually changes from the left and right sides of the tunnel to the upper and lower sides, consistently with the direction of the maximum external stress.

The differences in the spatial distribution of the AE event for different lateral pressure coefficients reflect the control effect of the stress conditions on the failure area around the tunnel. The results of this study are consistent with those of Ref. [42]; the author performed numerical simulations on the progressive fracturing processes around underground tunnels with different lateral pressure coefficients. In the case of $k=0.75$, the stress that concentrates in the left and right sides of the tunnel is higher than that in the upper and lower sides, causing the resulting damage to be mainly concentrated on the left and right sides (Figs. 8(a) and 8(c)). For the stress condition of $k=1.0$, the concentrated stress and damage are evenly distributed around the tunnel (Figs. 8(b) and (d)). The above studies show that the external stress controls the failure area and morphology around the tunnel. The blast disturbance cannot fundamentally change the failure area but will deepen the extent of damage and accelerate the failure speed. In underground tunnel engineering, the distribution of ground stress should determine

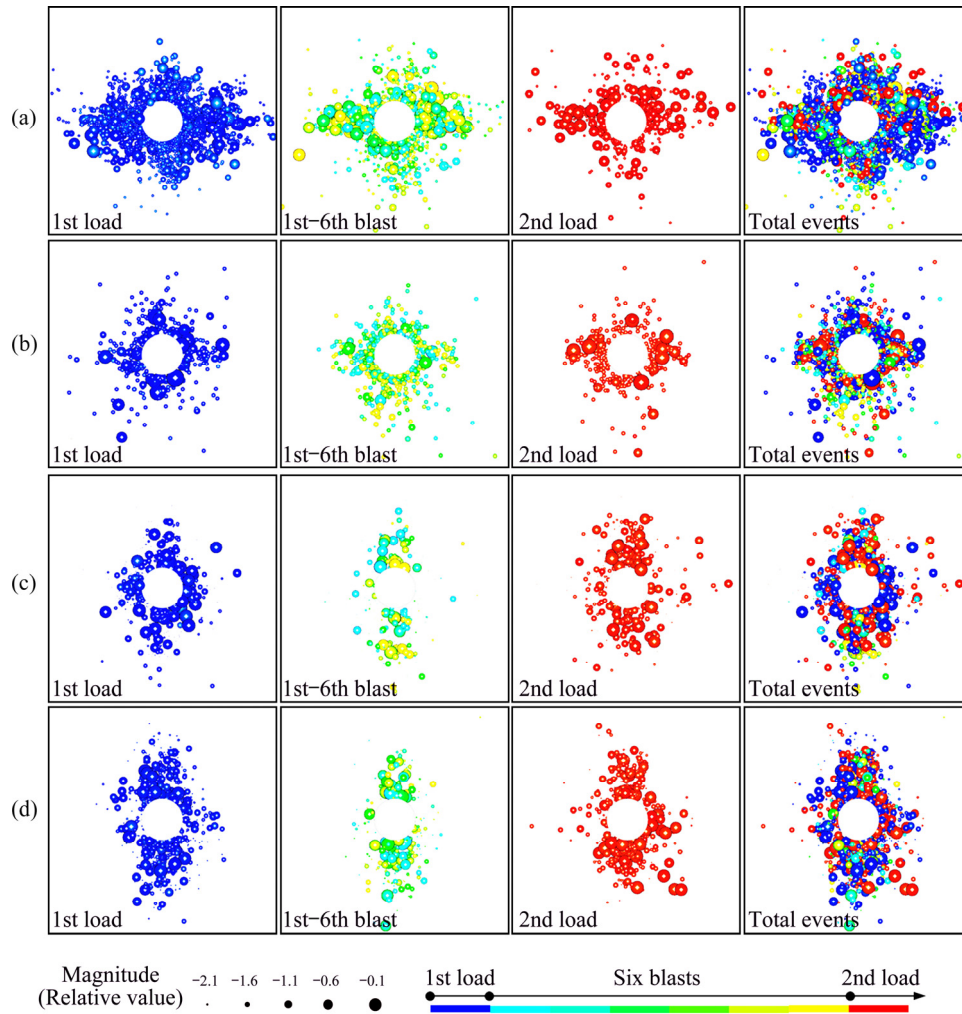


Fig. 7 Spatial distribution of AE events under loading and blast disturbances in specimens with different lateral pressure coefficients: (a) $k=0.8$; (b) $k=1.0$; (c) $k=1.2$; (d) $k=1.4$

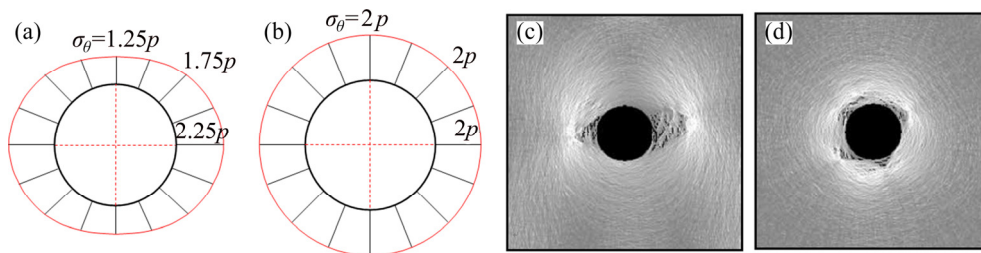


Fig. 8 Theoretical results of tangential stress (σ_θ) distribution and numerical simulation results of failure patterns around circular openings modified from ZHU et al [42]: (a) Stress distribution with $k=0.75$; (b) Stress distribution with $k=1.0$; (c) Failure pattern with $k=0.75$; (d) Failure pattern with $k=1.0$

the support area, while the supported depth should be considered comprehensively by taking the ground stress conditions and blast disturbance into account.

4.2 Evolution of apparent stress and displacement within specimens

The waveform information of AE signals can provide a deep interpretation of the stress field and

displacement field distribution during the specimen fracturing. The apparent stress is equal to half of the sum of the initial and final stresses, which supplies an estimate of the stress drop (or stress release) associated with a seismic event. High apparent stress values are indicative of high and increasing stress conditions within the rock mass, and vice versa [43,44]. Similar to the apparent stress, the apparent volume depends on the seismic potency

and radiated energy, and because of its scalar nature, it can easily be manipulated in the form of cumulative or contour plots [45]. Therefore, studies of the stress and displacement distribution and evolution law during the rock mass failure process are feasible. Based on the analysis of the microseismic data, the stress and displacement distributions and evolutions have been widely used to assess the rock mass stability and forecast dynamic hazards to manage disastrous rock failures [46–51] better.

WYSS and BRUNE [52] defined the apparent stress as the ratio of the total radiated seismic energy to the seismic moment:

$$\sigma_a = \mu(E/M_0) \tag{7}$$

where σ_a is the apparent stress, μ is the modulus of rigidity of the source, E is the radiated seismic energy, and M_0 is the seismic moment. The deformation parameter of the MS source can quantitatively describe the change in the rock mass deformation too. According to seismology, the relationship between the average displacement \bar{u} of the fault and seismic moment M_0 by AKI [53] is as follows:

$$M_0 = \mu \bar{u} S \tag{8}$$

where S is the area of the fault, and $S = \pi r_0^2$ (r_0 is the source radius). The seismic moment M_0 , radiated seismic energy E , and source radius r_0 are all obtained from the waveform.

Figures 9 and 10 show the distributions of

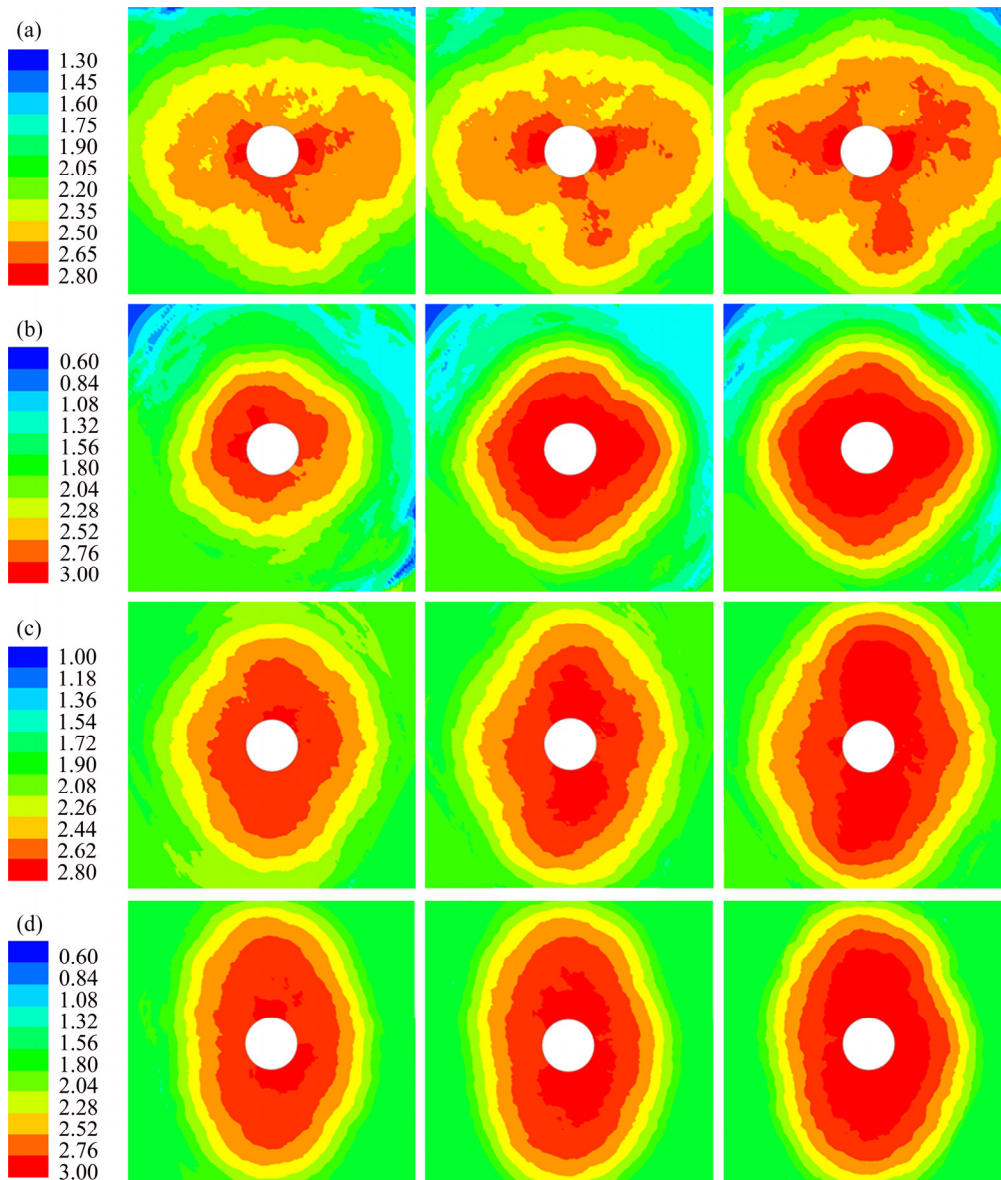


Fig. 9 Distribution of $\lg \sigma_a$, under loading and blast disturbances in specimens with different lateral pressure coefficients: (a) $k=0.8$; (b) $k=1.0$; (c) $k=1.2$; (d) $k=1.4$

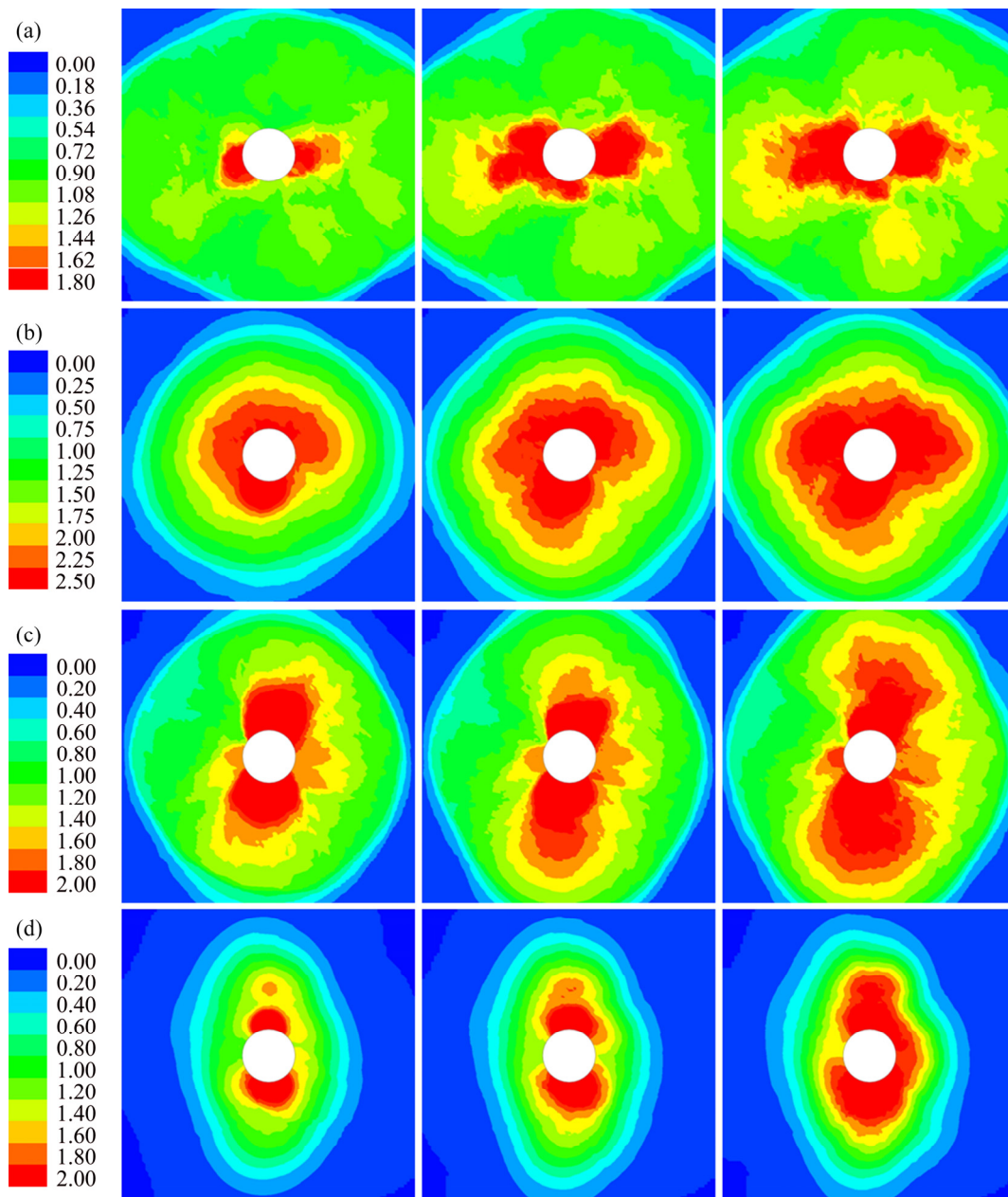


Fig. 10 Distribution of displacement under loading and blast disturbances in specimens with different lateral pressure coefficients: (a) $k=0.8$; (b) $k=1.0$; (c) $k=1.2$; (d) $k=1.4$

apparent stress and displacement in specimens with different lateral pressure coefficients, respectively. Because the unit of the AE signals detected during the experiment is voltage, i.e., mV, the AE source parameters, including the seismic moment, radiated seismic energy, apparent stress, and displacement, are all relative values, rather than absolute values. Therefore, the results of the size of AE events, the apparent stress, and the displacement distribution are also shown as relative values. In the case of $k=0.8$, the apparent stress is concentrated around the circular opening in the first loading process, with

the most significant stress concentrations on the left and right sides. At the same time, there are distinct areas of large displacement on both sides of the tunnel, which indicates that the stress exceeds the failure strength in some areas, leading to microcracks generation and large local deformation. After six blast disturbances, the stress slightly transferred and redistributed; the overall distribution remains unchanged, but the deformation area is expanded. After the secondary loading, the stress concentration and large deformation area around the tunnel further expand. For the specimen with $k=1.0$,

the stress has an approximately circular concentration region around the circular opening in the first loading process; it further expands due to the blast disturbance and the second loading. In this process, the evolution of the region of large displacement is consistent with that of stress concentration. Distribution and evolution characteristics of the stress field and displacement field of specimens with lateral pressure coefficients of 1.2 and 1.4 are similar to those of $k=0.8$ but are rotated by 90° . The above researches on the distribution and evolution of stress fields based on AE monitoring are consistent with ZHU et al [42], further verifying the control effect of the external load on the stress and damage distribution around the tunnel.

Note that the distributions of stress and displacement are consistent, indicating that the specimen is fairly homogeneous. Because the changes in the stress and displacement were independently obtained from the waveform, they can reflect the difference in the physical mechanics among different regions within the rock mass. The source of an event associated with a weaker geological feature or with a softer patch in the rock mass radiates less seismic energy per unit of inelastic co-seismic deformation than an equivalent source within strong and highly stressed rock mass. The phenomenon of increasing deformation and decreasing stress indicates that the rock mass degrades. In contrast, the integrity of

the rock mass is much better. For underground engineering, the integrity and degradation degree of the rock mass can be evaluated by distributions of stress and displacement calculated from AE or MS monitoring and provide a basis for determining the most appropriate control measures for hazards with different occurrence mechanisms.

5 Numerical simulation of tunnel damage

In addition to the experimental study on fracture processes round tunnels, a numerical simulation was performed with the FLAC^{3D} commercial software. The generated 3D model is $30\text{ m} \times 30\text{ m} \times 15\text{ m}$ ($L \times H \times W$), the radius of the tunnel is 2 m. To obtain small changes in the plastic zone around the tunnel, the meshing side length near the tunnel is 0.1 m, and the total number of units in the numerical model is 288000 (Fig. 11(a)). The physical and mechanical parameters of the rock mass came from Ashele copper mine data and were modified according to the Hoek–Brown strength criterion (Table 4). The Mohr–Coulomb constitutive model was used. During static loading, displacement constraints were applied on all six sides of the model, and the viscous boundary condition was adopted on the left, right, front, back, and bottom boundaries to absorb waves when the dynamic disturbance was performed. The parameters of the dynamic disturbance are derived

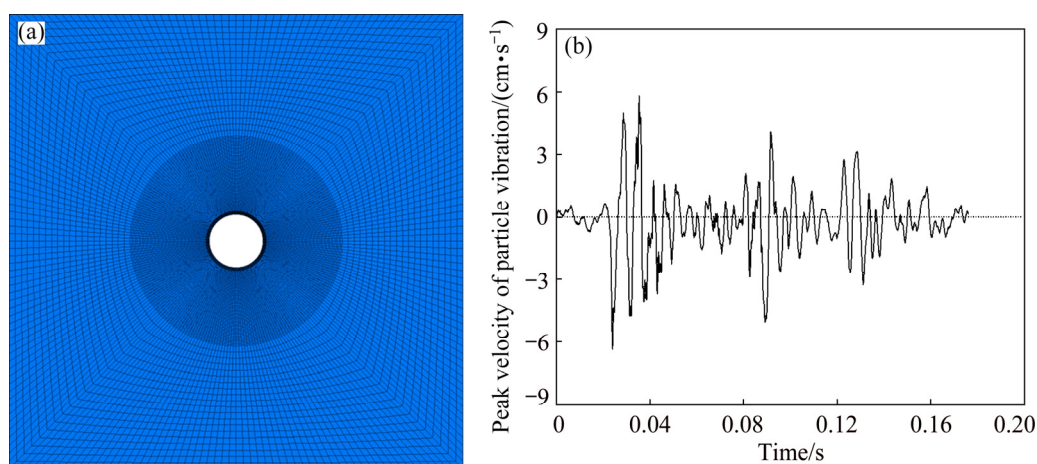


Fig. 11 Numerical simulation program: (a) Analysis model; (b) Blast vibration signal in field test

Table 4 Main physical and mechanical parameters of rock mass

Rock mass	Tensile strength/MPa	Elasticity modulus/GPa	Cohesion/MPa	Frictional angle/(°)	Volume weight/($\text{kN} \cdot \text{m}^{-3}$)	Poisson ratio
Tuff	0.16	11.46	0.51	31.26	27.41	0.25

from the test data of blast vibration measured at the No. 4 stope at the 0 m level (approximately 900 m in mining depth) in the Ashele copper mine (Fig. 11(b)). The blast signal was converted into a stress–time history curve according to the following formula:

$$\sigma_n = -2(\rho C_p)V_n \quad (9)$$

where ρ is the rock mass density, kg/m^3 ; C_p is the propagation velocity of the P wave in the rock mass, m/s ; V_n is the normal velocity component at the model boundary, m/s . The dynamic disturbance,

lasting 0.178 s, was performed at the bottom of the numerical model. In the numerical simulation, the horizontal stress was maintained at 30 MPa, and the vertical stress changed; thus, the investigated lateral pressure coefficients were 0.6, 0.8, 1.0, 1.2, and 1.4.

The numerical results show that the stress distribution and plastic zone range vary significantly with the lateral pressure coefficient (Fig. 12). Under static stress conditions, when k is smaller than 1.0, the maximum principal stress mainly concentrates on the left and right sides and is relatively low in the roof and floor of the tunnel.

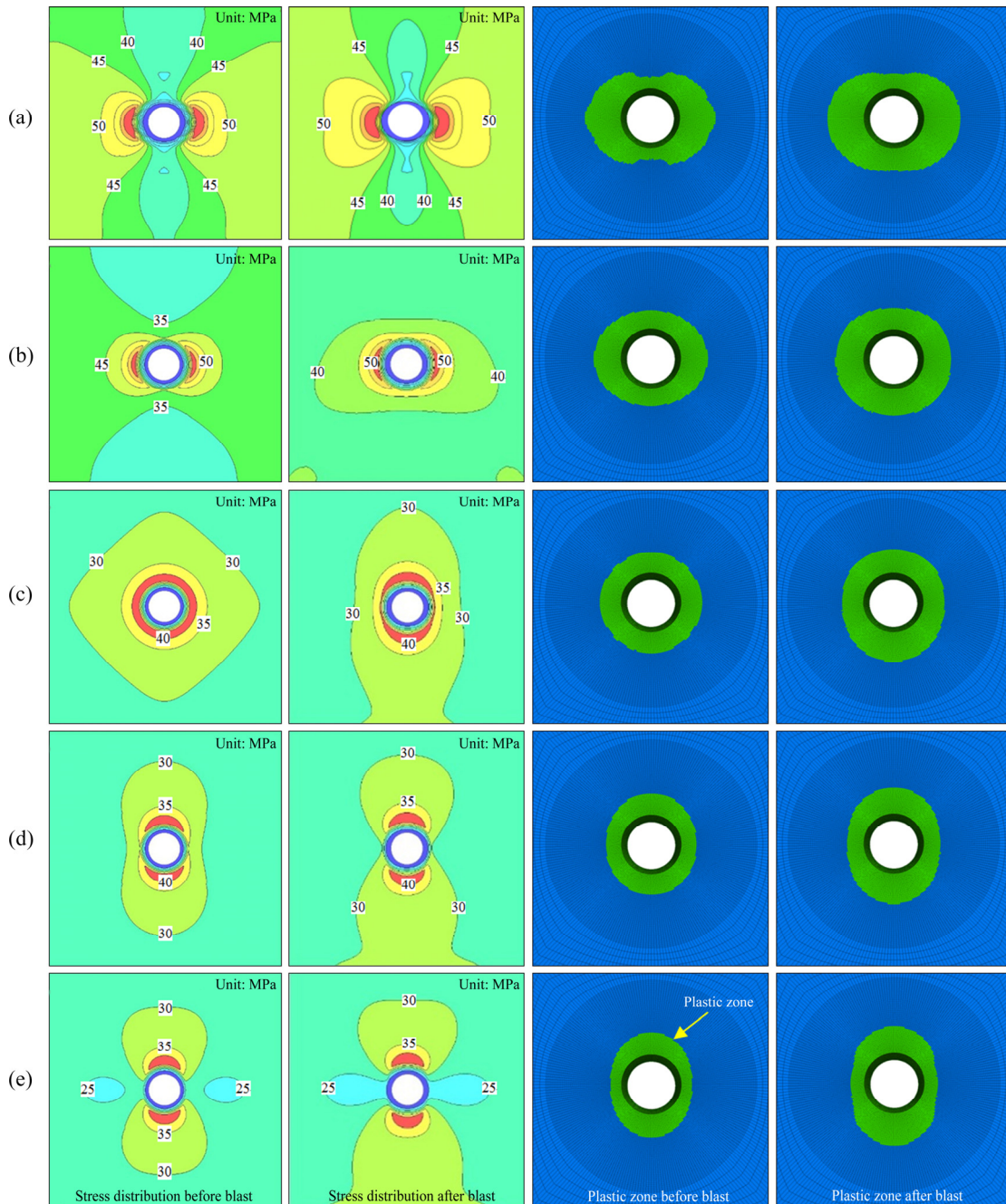


Fig. 12 Distribution of maximum principal stress and plastic zone before and after blast disturbance with different lateral pressure coefficients: (a) $k=0.6$; (b) $k=0.8$; (c) $k=1.0$; (d) $k=1.2$; (e) $k=1.4$

With the increase in the lateral pressure coefficient, the regions of stress concentration in the left and right sides gradually reduce, while they enlarge in the roof and floor regions. For $k=1.0$, the shape of the maximum principal stress concentration area has almost a circular shape. For $k>1.0$, the area of maximum principal stress mainly concentrates on the roof and floor regions, similar to the stress concentration area of $k<1.0$, but it has a 90° rotation. On the other hand, the plastic zone has an elliptical distribution, and it changes similarly to the stress concentration, i.e., the direction of the longer axis of the ellipse changes from horizontal to vertical direction with the increase in lateral pressure coefficients. For example, the depth of the plastic zone is 2.4 m in the two sidewalls and 0.7 m in the roof and floor when $k=0.6$. Conversely, the depth of the plastic zone is 0.7 m in the two sidewalls and 1.5 m on the roof and floor in the case of $k=1.4$. Note that the surrounding rock mass around the tunnel undergoes a visible stress relaxation phenomenon, and the area of the plastic zone is much larger than that of the relaxation zone. The concentrated stress around the tunnel has exceeded the failure strength of the rock mass, resulting in the rock mass lost its bearing capacity, thus forming a relaxation zone. Although the rock mass outside the relaxation zone is in a plastic state, it still has a bearing capacity under the radial constraint.

A dynamic disturbance enlarges the areas of the maximum principal stress concentration in the case of $k=0.6, 0.8, 1.2$, and 1.4 , respectively. For $k=1.0$, as the dynamic disturbance was applied at the bottom of the model, the areas of stress concentration in the roof and floor remarkably enlarge, which results in the stress being no longer uniform around the tunnel. Also, the areas of the plastic zone with different lateral pressure coefficients increase to different extents after the dynamic disturbance. For example, the areas of the plastic zone in the roof increase 0.3 m and 0.2 m, respectively, when the lateral pressure coefficients are 0.6 and 1.0, while there are no obvious changes in the two sidewalls. For $k=1.4$, the plastic zone in the roof and sidewall increases by 0.9 and 0.2 m, respectively. The volume increments of the plastic zone with different lateral pressure coefficients are 49.29, 28.74, 22.17, 23.65, and 24.87 m^3 , respectively (Table 5). This indicates that the

dynamic disturbance has the smallest impact on the tunnel when $k=1.0$. Moreover, the greater the difference between vertical and horizontal stresses, the greater the impact of dynamic disturbance on the tunnel. The results of the numerical simulation are consistent with the experimental results, that is, the external load dominates the damage zone distribution around the tunnel, and the blast disturbance significantly affects the damage depth.

Table 5 Volume changes in plastic zone before and after dynamic disturbance with different lateral pressure coefficients

k	Volume of plastic zone/ m^3		
	After loading	After blast	Increment
0.6	153.01	202.29	49.29
0.8	129.84	158.57	28.74
1.0	118.74	140.91	22.17
1.2	104.18	127.83	23.65
1.4	92.41	117.28	24.87

6 Conclusions

(1) The differences in the spatial distributions of the AE events for different lateral pressure coefficients reflect the control of stress conditions on the failure area around the tunnel. The blast disturbance cannot change the failure area but will deepen the damage and accelerate the failure speed.

(2) The AE activity is closely related to stress loading and blast disturbance. If more blasts are performed, the dynamic disturbance may cause more significant damage, and the specimens may be much more likely to fail during blast disturbance. The AE activity recovers to a relatively stable state within a short time after blast and conforms to power-law characteristics, which can be used to quantitatively determine the timing of stress adjustment in the rock mass. The distribution of the apparent stress calculated from AE data is consistent with the theoretical and numerical results, indicating that it can be used to evaluate the stress level within the rock mass.

(3) The more significant the difference between the vertical and horizontal stresses, the higher the impact on the tunnel by dynamic disturbance. The dynamic disturbance has the

smallest impact on the tunnel when the lateral pressure coefficient is 1.0. Under static load and dynamic disturbance, the area of the plastic zone is much larger than that of the relaxation zone. In tunnel engineering, the relaxation zone reinforced with a support can provide the radial constraint on the plastic zone, which helps to maintain the bearing capacity of the rock mass.

References

- [1] LI Xi-bing, YAO Jin-rui, GONG Feng-qiang. Dynamic problems in deep exploitation of hard rock metal mines [J]. *The Chinese Journal of Nonferrous Metals*, 2011, 21(10): 2551–2563. (in Chinese)
- [2] MARTINO J B, CHANDLER N A. Excavation-induced damage studies at the underground research laboratory [J]. *International Journal of Rock Mechanics and Mining Sciences*, 2004, 41(8): 1413–1426.
- [3] DOERNER C A C. Quantifying the effect of rock mass quality on peel particle velocity for underground drift development [D]. Columbia: University of British Columbia, 2011.
- [4] JIANG Nan, ZHOU Chuan-bo, LUO Xue-dong, LU Shi-wei. Damage characteristics of surrounding rock subjected to VCR mining blasting shock [J]. *Shock and Vibration*, 2015, 1–8.
- [5] LIU Jian-po, XU Shi-da, LI Yuan-hui. Analysis of rock mass stability according to power-law attenuation characteristics of acoustic emission and micro activities [J]. *Tunnelling and Underground Space Technology*, 2019, 83(1): 303–312.
- [6] LIU Jian-po. Studies on relationship between microseism time-space evolution and ground pressure activities in deep mine [D]. Shenyang: Northeastern University, 2011. (in Chinese)
- [7] FENG Xia-ting, CHEN Bing-rui, ZHANG Chuan-qing, LI Shao-jun, WU Shi-yong. Mechanism, warning and dynamic control of rockburst development process [M]. Beijing: Science Press, 2013. (in Chinese)
- [8] ZHU Wan-cheng, ZUO Yu-jun, SHANG Shi-ming, LI Zhan-hai, TANG Chun-an. Numerical simulation of instable failure of deep rock tunnel triggered by dynamic disturbance [J]. *Chinese Journal of Rock Mechanics and Engineering*, 2007, 26(5): 915–921. (in Chinese)
- [9] HOMAND-ETIENNE F, HOXHA D, SHAO Jian-fu. A continuum damage constitutive law for brittle rocks [J]. *Computers and Geotechnics*, 1998, 22(2): 135–151.
- [10] ZHANG Zong-xian, KOU Shao-quan, YU Jun-hong, JINAG L G, LINDQVIST P A. Effects of loading rate on rock fracture [J]. *International Journal of Rock Mechanics and Mining Sciences*, 1999, 36(5): 597–611.
- [11] YANG Xiao-lin, YUAN Xiao-you, WU Zhong, SU Cheng-dong. Experimental study on mechanical properties of blasting damaged rock [J]. *Chinese Journal of Rock Mechanics and Engineering*, 2001, 20(4): 436–439. (in Chinese)
- [12] HE Man-chao, LIU Dong-qiao, GONG Wei-li, WANG Cheng-chao, KONG Jie, DU Shuai, ZHANG Shen. Development of a testing system for impact rockbursts [J]. *Chinese Journal of Rock Mechanics and Engineering*, 2014, 33(9): 1729–1739. (in Chinese)
- [13] GU Jin-cai, CHEN An-min, XU Jing-mao, ZHAO Hong-ling, ZHANG Yang, GU Lei-yu. Model test study of failure patterns of anchored tunnel subjected to explosion load [J]. *Chinese Journal of Rock Mechanics and Engineering*, 2008, 27(7): 1315–1320. (in Chinese)
- [14] ZHANG Feng-peng, PENG Jian-yu, FAN Guang-hua, LI Shao-jun, LI Yuan-hui. Mechanisms of blasting-induced rock fractures under different static stress and joint properties conditions [J]. *Rock and Soil Mechanics*, 2016, 37(7): 1839–1846. (in Chinese)
- [15] LI Yuan-hui, PENG Jian-yu, ZHANG Feng-peng, QIU Zhao-guo. Cracking behavior and mechanism of sandstone containing a pre-cut hole under combined static and dynamic loading [J]. *Engineering Geology*, 2016, 213(4): 64–73.
- [16] PENG Jian-yu, LI Yuan-hui, ZHANG Feng-peng, QIU Zhao-guo. Failure process and mechanism of sandstone under combined equal biaxial static compression and impact loading [J]. *Strain*, 2018, 54: 1–12.
- [17] ZHU Wan-cheng, LI Zhan-hai, ZHU Li-kai, TANG Chun-an. Numerical simulation on rockburst of underground opening triggered by dynamic disturbance [J]. *Tunnelling and Underground Space Technology*, 2010, 25(5): 587–599.
- [18] LI Xi-bing, LI Ching-jin, CAO Wen-zhuo, TAO Ming. Dynamic stress concentration and energy evolution of deep-buried tunnels under blasting loads [J]. *International Journal of Rock mechanics and Mining Sciences*, 2018, 104: 131–146.
- [19] MOGI K. Earthquake and fracture [J]. *Tectonophysics*, 1967, 5: 35–55.
- [20] SCHOLZ C H. The frequency–magnitude relation of microfracturing in rock and its relation to earthquakes [J]. *Bulletin of Seismological Society of America*, 1968, 58(1): 399–415.
- [21] OHTSU M. Simplified moment tensor analysis and unified decomposition of acoustic emission source: Application to in situ hydro fracturing test [J]. *Journal of Geophysical Research*, 1991, 96: 6211–6221.
- [22] LOCKNER D A. The role of acoustic emission in the study of rock fracture [J]. *International Journal of Rock mechanics and Mining Sciences and & Geomechanics Abstracts*, 1993, 30(7): 883–899.
- [23] CHANG S H, LEE C I. Estimation of cracking and damage mechanisms in rock under triaxial compression by moment tensor analysis of acoustic emission [J]. *International Journal of Rock mechanics and Mining Sciences*, 2004, 41(7): 1069–1086.
- [24] LEI Xing-lin, SATOH T. Indicators of critical point behavior prior to rock failure inferred from pre-failure damage [J]. *Tectonophysics*, 2007, 431(1–4): 97–111.
- [25] CAI Ming, MORIOKA H, KAISER P K, TASAKA Y, KUROSE H, MINAMI M, MAEJIMA T. Back-analysis of rock mass strength parameters using AE monitoring data [J].

- International Journal of Rock mechanics and Mining Sciences, 2007, 44(4): 538–549.
- [26] LI Yuan-hui, LIU Jian-po, ZHAO Xing-dong, YANG Yu-jiang. Experimental studies of the change of spatial correlation length of acoustic emission events during rock fracture process [J]. International Journal of Rock mechanics and Mining Sciences, 2010, 47(8): 1254–1262.
- [27] XU S, LIU Jian-po, XU Shi-da, WEI Jiong, HUANG Wen-bo, DONG Long-bin. Experimental studies on pillar failure characteristics based on acoustic emission location technique [J]. Transactions of Nonferrous Metals Society of China, 2012, 22(11): 2792–2798.
- [28] DONG Long-jun, LI Xi-bing, ZHOU Zi-long, CHEN Guang-hua, MA Ju. Three-dimensional analytical solution of acoustic emission source location for cuboid monitoring network without pre-measured wave velocity [J]. Transactions of Nonferrous Metals Society of China, 2015, 25(1): 293–302.
- [29] DU Kun, LI Xi-bing, LI Di-yun, WENG Lei. Failure properties of rocks in true triaxial unloading compressive test [J]. Transactions of Nonferrous Metals Society of China, 2015, 25(2): 571–581.
- [30] LIU Xi-ling, LUO Ke-bing, LI Xi-bing, LI Qi-yue, WANG Wei-hua, GONG Feng-qiang. Cap rock blast caving of cavity under open pit bench [J]. Transactions of Nonferrous Metals Society of China, 2017, 27(3): 648–655.
- [31] LUO Zhou-quan, WANG Wei, QIN Ya-guang, XIANG Jun. Early warning of rock mass instability based on multi-field coupling analysis and microseismic monitoring [J]. Transactions of Nonferrous Metals Society of China, 2019, 29(6): 1285–1293.
- [32] ZHOU Zi-long, ZHOU Jing, CAI Xin, RUI Yi-chao, CHEN Lian-jun, WANG Hai-quan. Acoustic emission source location considering refraction in layered media with cylindrical surface [J]. Transactions of Nonferrous Metals Society of China, 2020, 30(3): 789–799.
- [33] DONG Long-jun, WESSELOO J, POTVIN Y, LI Xi-bing. Discrimination of mine seismic events and blasts using the fisher classifier, naive Bayesian classifier and logistic regression [J]. Rock Mechanics and Mining Sciences, 2016, 49(1): 183–211.
- [34] MA Ju, DONG Long-jun, ZHAO Guo-yan, LI Xi-bing. Discrimination of seismic sources in an underground mine using full waveform inversion [J]. International Journal of Rock Mechanics and Mining Sciences, 2018, 106: 213–222.
- [35] XIAO Ya-xun, FENG Xia-ting. Neural network for noise filtering of microseismicity monitoring in tunnels [C]// Rockburst 2018. Amsterdam: Elsevier, 2018: 317–323.
- [36] FUTTERMAN W I. Dispersive body waves [J]. Journal of Geophysical Research, 1962, 67(13): 5279–5291.
- [37] OMORI F. On the after-shocks of earthquakes [J]. Journal of the College of Science, Imperial University of Tokyo, 1894, 7: 111–200.
- [38] UTSU T. Aftershocks and earthquake statistics (I): Some parameters [J]. Geophysics, 1958, 3: 129–195.
- [39] HIRATA T. Omori's power law aftershock sequences of microfracturing in rock fracture experiment [J]. Journal of Geophysical Research: Solid Earth, 1987, 92(B7): 6215–6221.
- [40] KATSUYAMA K. Application of AE techniques [M]. FENG Xia-ting, trans. Beijing: Metallurgy Industry Press, 1996.
- [41] PRUGGER A F, GENDZWILL D J. Microearthquake location: a nonlinear approach that makes use of a simplex stepping procedure [J]. Bulletin of Seismological Society of America, 1988, 78: 799–815.
- [42] ZHU Wan-cheng, LIU Ji-shan, TANG Chun-an, ZHAO Xing-dong, BRADY B H. Simulation of progressive fracturing processes around underground excavations under biaxial compression [J]. Tunnelling and Underground Space Technology, 2005, 20(3): 231–247.
- [43] MENDECKI A J. Real time quantitative seismology in mine [C]//Rockbursts and Seismicity in Mines. YOUNG R P, ed. Balkema, Rotterdam, 1993: 287–296.
- [44] BROWN L G, HUDYMA M R, TURCOTTE P. Seismic hazard assessment using apparent stress ratio [C]//Underground Design Methods. Perth, Australian: Australian Centre for Geomechanics, 2015: 123–134.
- [45] MENDENCKI A J. Seismic monitoring in mines [M]. London: Chapman & Hall, 1997.
- [46] GIBOWICZ S J. An anatomy of a seismic sequence in a deep gold mine [J]. Pure and Applied Geophysics, 1997, 150(3–4): 393–414.
- [47] GE M C. Efficient mine microseismic monitoring [J]. International Journal of Coal Geology, 2005, 64(1–2): 44–56.
- [48] TANG Li-zhong, WANG Ling-hui, ZHANG Jun, LI Xi-bing. Seismic apparent stress and deformation in a deep mine under large-scale mining and areal hazardous seismic prediction [J]. Chinese Journal of Rock Mechanics and Engineering, 2011, 30(6): 1168–1178. (in Chinese)
- [49] LIU Jian-po, FENG Xia-ting, LI Yuan-hui, XU Shi-da, SHENG Yu. Studies on temporal and spatial variation of microseismic activities in a deep metal mine [J]. International Journal of Rock Mechanics and Mining Sciences, 2013, 60: 171–179.
- [50] MA Tian-hui, TANG Chun-an, TANG Lie-xian, ZHANG Wen-long, WANG Long. Mechanism of rock burst forecasting based on micro-seismic monitoring technology [J]. Chinese Journal of Rock Mechanics and Engineering, 2016, 35(3): 470–482. (in Chinese)
- [51] BROWN L, HUDYMA M. Identification of stress change within a rock mass through apparent stress of local seismic events [J]. Rock Mechanics and Rock Engineering, 2017, 50(1): 81–88.
- [52] WYSS M, BRUNE J N. Seismic moment, stress and source dimensions for earthquakes in the California-Nevada region [J]. Journal of Geophysical Research, 1968, 73(14): 4681–4694.
- [53] AKI K. Estimation of earthquake moment, released energy, and stress-strain drop from G wave spectrum [J]. Bulletin of the Earthquake Research Institute, 1966, 44: 73–88.

不同侧压力系数条件下 爆破扰动诱发巷道渐进破裂过程

龙翼, 刘建坡, 雷刚, 司英涛, 张长银, 魏登铨, 师宏旭

东北大学 深部金属矿山安全开采教育部重点实验室, 沈阳 110819

摘要: 采用实验和数值模拟相结合的方法研究静应力和爆破扰动所诱发的巷道围岩渐进破裂过程。研究表明: 围岩的损伤程度由静应力加载和爆破动力扰动的双重作用所致, 不同侧压力系数条件下静应力加载和爆破动载扰动条件下巷道围岩损伤破坏具有明显的差异性。初始应力条件控制着巷道围岩破坏区域的分布特征, 爆破扰动会加剧巷道围岩的损伤深度和失稳破坏速度。垂向和水平静应力差值越大, 爆破扰动造成的巷道损伤程度越大。爆破结束后, 声发射活动在较短的时间内恢复到稳定状态, 且符合幂律衰减规律。

关键词: 巷道破坏; 爆破扰动; 侧压力系数; 声发射; 幂率拟合

(Edited by Xiang-qun LI)